

Experimental Study of the Bottleneck in Fully Developed Turbulence

Christian Küchler¹, Gregory Bewley², and Eberhard Bodenschatz^{1,2,3}

¹*Max-Planck-Institute for Dynamics and Self-Organization, Göttingen, Germany*

²*Cornell University, Ithaca, USA and*

³*Georg August University Göttingen, Germany*

The energy spectrum of incompressible turbulence is known to reveal a pileup of energy at those high wavenumbers where viscous dissipation begins to act. It is called the bottleneck effect [10, 11, 16, 26, 47]. Based on direct numerical simulations of the incompressible Navier-Stokes equations, results from Donzis & Sreenivasan [10] pointed to a decrease of the strength of the bottleneck with increasing intensity of the turbulence, measured by the Taylor micro-scale Reynolds number R_λ . Here we report first experimental results on the dependence of the amplitude of the bottleneck as a function of R_λ in a wind-tunnel flow. We used an active grid [17] in the Variable Density Turbulence Tunnel (VDTT) [3] to reach $R_\lambda > 5000$, which is unmatched in laboratory flows of decaying turbulence. The VDTT with the active grid permitted us to measure energy spectra from flows of different R_λ , with the small-scale features appearing always at the same frequencies. We relate those spectra recorded to a common reference spectrum, largely eliminating systematic errors which plague hotwire measurements at high frequencies. The data are consistent with a power law for the decrease of the bottleneck strength for the finite range of R_λ in the experiment.

I. INTRODUCTION

Turbulence is omnipresent in natural and technological flows. Its consequences for the associated processes are essential in the fields of astrophysics, geophysics, meteorology, biology, and in many engineering disciplines from chemical engineering, combustion science, heat and mass transfer engineering to aeronautics, marine science and renewable energy research. From the fundamental perspective the mathematical field theory of the incompressible Navier Stokes equation continues to challenge pure and applied mathematicians [14]. In turbulence fluid velocities and accelerations fluctuate greatly and any description can only be statistical in nature. It is believed that at very high turbulence levels at spatial scales smaller than the energy injection scale the turbulence shows universal properties, independent of the particular driving. According to Kolmogorov's phenomenology from 1941 [24] (abbreviated K41), the universal statistical spatial properties of fully developed turbulence can be captured in three ranges of spatial scales. Kinetic Energy is injected into the turbulent fluctuations at the largest scales, whose properties are particular to the driving mechanism. The kinetic energy is transformed into heat at the very smallest scales through viscous dissipation. If the range of spatial scales found in the turbulent structures is large enough, a third range of scales develops, where neither the peculiarities of energy injection, nor viscous dissipation influence the spatial scale-to-scale energy transfer. This range is called the inertial range. In this intermediate range statistical properties can be interpreted by the scale-to-scale transfer of kinetic energy only, described by the kinetic energy dissipation range ε (dissipated power per unit mass). The dimensionless quantity used to give the strength of turbulence and thus the size of the inertial range scaling is the Taylor

microscale Reynolds number

$$R_\lambda = \frac{u\lambda}{\nu}.$$

u is the rms of the velocity fluctuations, ν is the kinematic viscosity of the fluid, and λ is the Taylor microscale, which can be thought of as the smallest length scale at which molecular viscosity can be neglected [43]. It can therefore be interpreted as a typical size of an inertial range eddy. In statistically isotropic and homogeneous turbulence R_λ can be linked to the well-known Reynolds number $\text{Re} = uL/\nu$ based on the large scales L via $R_\lambda = \sqrt{15\text{Re}}$ [42]. The integral scale L can be estimated as the integral over the velocity correlation function $L_{11} = \int \langle u(x+r)u(r) \rangle dr$.

In K41 phenomenology for spatially homogeneous and statistically isotropic turbulence the spatial energy spectrum in the inertial range is given by

$$E(k) = C_K \varepsilon^{2/3} k^{-5/3}. \quad (1)$$

C_K is the Kolmogorov constant, k is the wavenumber. In this K41 spectrum the only free parameter is the dissipation rate ε as indicated above.

Despite its simplicity, Eq. (1) describes the energy spectrum of observed and simulated turbulent flows quite well (see [33] for a compilation). Nevertheless, important deviations are well known. When analyzing the compensated spectrum, $E(k)\varepsilon^{-2/3}k^{5/3}$, deviations from a $k^{-5/3}$ scaling are found. Prominent is an increase in amplitude of the compensated spectrum at the high-wavenumber end of the inertial range. This pileup of energy is commonly called the bottleneck effect [11, 16, 26, 46, 47, 52]. It has been observed in laboratory flows (e.g. [3, 33, 38?]) and direct numerical simulations (DNS) [10, 21–23] alike and is typically preceded by a distinct local minimum of the compensated spectrum. The bottleneck

peak is very shallow or almost absent in hot-wire measurements of atmospheric boundary layer turbulence at very high $R_\lambda > 10^4$ [18, 41, 44]. It is generally less pronounced in one-dimensional spectra than in three-dimensional ones [9]. The effect is also present in structure functions and influences the rapidity of the transition between the viscous and inertial ranges in the second-order structure function [10, 27], hints of which can also be found in structure functions of higher orders [39]. The most extensive analysis of the bottleneck effect has been performed by Donzis & Sreenivasan [10] on DNS at R_λ up to 1000. They found that the bottleneck effect can be characterized as the difference between the bottleneck peak height and the level of the preceding minimum in the compensated spectrum. They conclude that the bottleneck effect weakens as a function of R_λ and report a scaling of $R_\lambda^{-0.04}$. Furthermore, they find that the peak of the bump occurs around $k\eta \approx 0.13$ in three-dimensional spectra, independent of R_λ . Here η is the Kolmogorov length scale, where dissipative effects are expected to dominate.

From a theoretical perspective, various explanations exist for the bottleneck effect. Falkovich [11] showed that a small perturbation to a K41 spectrum in the energy transfer equation leads to a correction of the form $\delta E(k) = E(k)(k/k_p)^{-4/3} \ln^{-1}(k_p/k)$, where k_p is the bottleneck wavenumber. Kurien et al. [26] argued that the time scale of helicity can be comparable to the energy time scale in the inertial range, where the relative helicity is already weak. They propose that the bottleneck effect is a change in the scaling exponent of the energy spectrum from $-5/3$ to $-4/3$. Their DNS supports this claim as they find a corresponding scaling range in the three-dimensional spectrum. The scaling is absent in the one-dimensional versions of their spectra. Frisch et al. [16] studied hyperviscous Navier-Stokes equations (Laplacian of order $\alpha \geq 2$) and attribute the bottleneck effect to an incomplete thermalization of high-wavenumber modes in the spatial spectrum. None of these studies directly incorporates a R_λ -dependence of the bottleneck height. Verma & Donzis [47] study the nonlocal and nonlinear mode-to-mode energy transfer in a shell model of turbulence and find that a significant portion of the energy flux away from a wavenumber shell goes to distant shells. Thus an efficient energy cascade requires a large inertial range. If the inertial range is insufficient, the energy piles up at the dissipative drop-off. As the length of the inertial range is tightly linked to R_λ , this implies a dependence of the bottleneck intensity on the Reynolds number.

In summary, the bottleneck effect has been studied systematically in DNS and various models. Numerical simulations indicate that the effect gets weaker with increasing R_λ , which is also predicted by Verma & Donzis [47] and in agreement with atmospheric measurements at ultra-high R_λ , where it is absent.

Here we present a detailed analysis of the R_λ -scaling of the bottleneck effect over an unprecedented range of R_λ

in a well controlled laboratory flow. The analysis of the bottleneck effect from experimental data can be demanding as systematic errors can cloud the results. From the perspective of the measuring instrument a small bump in the compensated spectrum is a subtle effect that occurs at rather high frequencies not yet resolvable in PIV or PTV measurements and very difficult to achieve in LDV. We use classical constant temperature hot-wire anemometry (CTA) assuming Taylor frozen flow hypothesis [43] in the Max Planck Variable Density Turbulence Tunnel (VDTT) [3]. Even with very well-established hot-wire technology, subtle changes in the energy spectrum at high frequencies can be heavily influenced by amplification or attenuation at such frequencies (see Sec. II B for a review).

In this manuscript we work around those effects and investigate the bottleneck effect from the lowest Reynolds number at which it can be identified (~ 200) up to the highest R_λ ever measured in a wind tunnel flow.

The paper is organized as follows: First, we present a concise compilation of experimental efforts to reach high R_λ and describe the Variable Density Turbulence Tunnel. We continue with a brief review of challenges posed by constant temperature hot-wire anemometry, especially its frequency responses. In Sec. III we introduce the relative spectra that allow us to eliminate instrumentation errors to a large extent. Finally we report the results of our analysis and discuss their relevance for the scaling of the bottleneck effect with R_λ .

II. EXPERIMENTAL METHODS

A. High R_λ and the Variable Density Turbulence Tunnel

Kolmogorov's 1941 predictions of universal scaling in turbulent flows refer to the limit of large R_λ , such that the regimes of energy injection and viscous dissipation are well separated [24]. This condition is cumbersome to achieve practically. A large separation of scales and therefore a large R_λ is found in atmospheric flows [18, 41, 44], where control is impossible and stationary conditions are difficult to achieve. They are difficult to achieve in controlled laboratory flows, where all scales can be reliably measured. To reach high R_λ one can turn two knobs: the size of the energy injection scale L and the dissipation scale $\eta = (\nu^3/\varepsilon)^{1/4}$. In direct numerical simulations (DNS), a compromise between the size of the periodic box, (limiting L), the spatial and temporal resolution, the convergence time, and the available resources needs to be found. The largest $R_\lambda = 2340$ achieved in a DNS under these constraints to date has been performed by Ishihara [22]. The limits of computational capabilities in terms of resolution have been recently pointed out by Yeung et al. [53].

In a laboratory experiment the energy injection scale L is limited by the dimensions of the apparatus. Large ap-

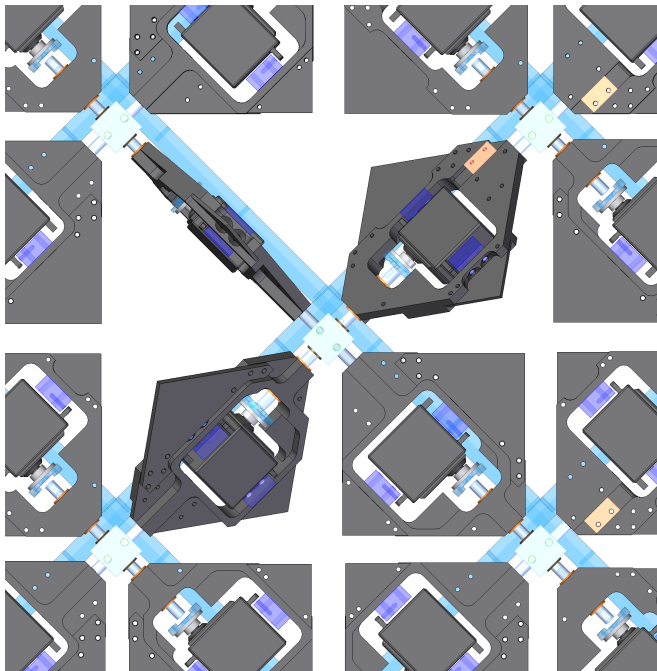


Figure 1. Several flaps of the active grid. The flow points out of the page. Starting from the top left flap in clockwise direction the flaps are set to 0° , 45° , 90° , and 45° . The side length of one flap is 11 cm, the black boxes in the flap center are servo motors, the blue rods are the grid support.

paratuses can be built, e.g. the Modane wind tunnel[5], but are prohibitively expensive to operate, especially considering the many realizations needed for dedicated statistical studies of turbulence. To expand the inertial range the dissipative scales of size $\sim \eta$ can be decreased by lowering the kinematic viscosity ν of the working fluid demanding a higher resolution of the measurement instrument. Examples for experiments in liquid helium, which has an ultra-low kinematic viscosity, are found for example in Refs. [31, 32, 35, 36]. The authors use liquid helium as working fluid in various flow configurations and have been reported to reach R_λ up to 10000. The dissipative scales of these flows are so small that they cannot be resolved by current technology

Our approach to create a large inertial range is to use a closed-loop wind tunnel filled with sulfur-hexafluoride (SF_6) at pressures up to 15 bar [3] - the Variable Density Turbulence Tunnel (VDTT). With classical grids it has been shown to create R_λ up to 1600 and Kolmogorov scales $\sim 10 \mu\text{m}$, making even the smallest spatial scales experimentally accessible [40]. With a specially designed autonomous active grid (see below) it is possible to increase the energy injection scale and thus the inertial range. As $R_\lambda \sim (L/\eta)^{3/4}$, the VDTT features two independent handles to change R_λ - pressure and active grid forcing. In combination they create a laboratory flow of R_λ more than 5000 at scales resolvable with modern thermal anemometry under the limitations described below.

The autonomous active grid consists of 111 individu-

ally controllable flaps of dimensions 11 cm x 11 cm that rotate around their diagonal. This is different from the Makita-style grids, where the rows and columns of the flaps are mounted rigidly on rotating horizontal and vertical bars [19]. The angle of rotation can be set to any angle between $\pm 90^\circ$. The flow obstruction is smallest (flap parallel to the flow) at 0° . At angles $\neq 0^\circ$ one of the flap sides is facing the incoming flow, while the other side is facing away from the flow. The sign of the angles determines the side that is facing the flow, while the magnitude defines the deviation of the flap from the parallel position. As in a classical grid with rigid grid bars, wakes are formed that interact with each other downstream of the grid to form a turbulent flow field. The flexibility of the grid allows the superposition of larger structures onto those induced by the individual flaps. A detailed account of the autonomous active grid and the algorithm is given in Ref. [17] and briefly summarized here.

The algorithm updates the angle of each flap every 0.1s. Each time step starts with a random set of angles and convolves each of those angles with the history and a pre-defined kernel. The kernel is always defined by a certain shape (e.g. Gaussian), the spatial and temporal correlations (the number of neighbors and time-steps included in the convolution), and the desired mean absolute angle ϕ_{RMS} . More complex kernel shapes require additional parameters. For the experiments presented here, a 'Long Tail' kernel has been used, which reduces the correlation with neighboring flaps and therefore emphasizes the correlation of the angle with its own past.

This algorithm leads to dynamically evolving patches of more open and more closed flaps without periodicity. The typical time- and length scales of those patches are controlled by the spatial and temporal correlation lengths, σ_s and σ_t , respectively, and the mean flap angle ϕ_{RMS} defines their mean amplitude. We describe the correlation as a box of dimensions $\sigma_s \times \sigma_s \times (\sigma_t \cdot U)$ and relate this volume V_{Corr} to the energy injection scales $L = \int C(r) dr$ in Fig. 2 a. As expected, larger correlation volumes lead to larger energy injection scales, with a corresponding change in R_λ . σ_s and σ_t can be set independently, but to avoid a strongly inhomogeneous flow they are typically linked via the mean flow velocity U forming a cubic correlation box: $\sigma_t \cdot U \approx \sigma_s$. This rule-of-thumb needs to be relaxed slightly to achieve $R_\lambda > 3000$ leading to a correlation box that is elongated in the σ_t direction.

The grid parameters can be distilled further into a grid Reynolds number. The relevant length scale is given by $\sqrt[3]{V_{\text{Corr}}}$, which corresponds to σ_s in the case of a cubic correlation box. The fluctuating velocity is proportional to the mean flow velocity and the mean angle amplitudes ϕ_{RMS} :

$$\text{Re}_{\text{Grid}} \sim \frac{\sqrt[3]{V_{\text{Corr}}}(\phi_{RMS}U)}{\nu},$$

where U is the mean flow velocity of the VDTT and ν the kinematic viscosity. Fig. 2 b) shows that the *a priori* quantity Re_{Grid} scales with the *a posteriori* R_λ with devi-

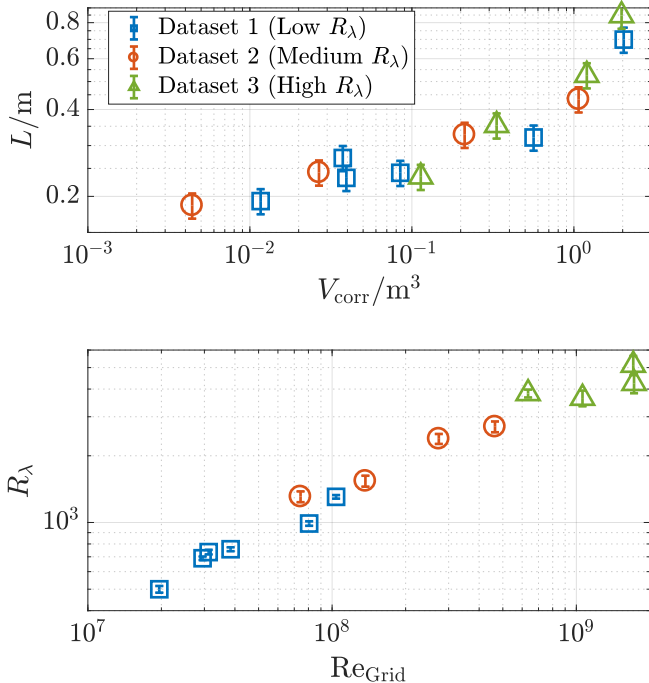


Figure 2. (a) The correlation volume $V_{\text{corr}} = \sigma_s^2 \sigma_t U$ influences the size of the largest scales L . (b) The grid Reynolds number defined as $\text{Re}_{\text{Grid}} = \sqrt[3]{V_{\text{corr}}} \phi_{\text{RMS}} U / \nu$ determines R_λ . The flattening of the individual Datasets indicate a limit to the increase of R_λ through the active grid. The first spectrum of Dataset 1 is not shown, because V_{corr} is not defined for a stationary, open grid.

ations at $\text{Re}_{\text{Grid}} > 10^9$. Each Dataset has been obtained by increasing V_{corr} while keeping the pressure (and therefore ν constant) as indicated in Tab. I. We attribute the slight deviations at large Re_{Grid} from a power law dependence to the fact that L is approaching half the diameter of the measurement section. This is a natural limit for a sensible energy injection in any tunnel. We would like to add the word of caution that when approaching this limit, isotropy and homogeneity cannot be assumed easily anymore, which leads to said deviations from the isotropic relation $R_\lambda \sim \text{Re}_{\text{Grid}}^\zeta$ with $\zeta \approx 0.5$. Nevertheless, these data confirm that the active grid is indeed another ‘knob’ to change R_λ through the large scales.

B. Thermal Anemometry

More than a century after its invention [8], hot-wire anemometry remains the technique of choice to measure the energy spectrum of turbulent velocity fluctuations in a strong mean flow. Constant temperature anemometry is responsive to fluctuations up to very high frequencies. The sensing element’s resistance - and therefore its temperature - is kept constant by a feedback circuit. As long as the feedback circuit is fast enough, the thermal lag of

the wire does not attenuate fluctuations faster than the thermal time scale of the wire. This comes at the expense of a more complicated circuitry and frequency response.

The frequency response of CTA circuits has been studied extensively both through theoretical models and experimental testing. Freymuth [15] linearized a circuit with a single feedback amplifier of infinitely flat frequency response and analyzed its response to square and sine waves. He finds that the system can be modeled by a third-order ODE if the circuit responds faster than the wire, and the frequency response is optimal (flat over the entire range of frequencies) when the system response to a step perturbation by a single, slight overshoot (critically damped system). Perry & Morrison [30] investigated more moderate amplifier gains and bridge imbalances in their study yielding similar results. Wood [50] expanded the Perry & Morrison analysis, but considered a single-stage amplifier with a frequency-dependent response. Watmuff [48] further expanded the model with multiple, non-ideal amplifier stages. He showed that at least two amplifier stages are necessary to model the real amplifier properly. This introduces two additional poles to the system and makes the frequency response more complicated. Samie et al. [37] recently studied anemometry with sub-miniature probes in this model and compared it to a real CTA measurement. The results supported the further development of their in-house circuit, such that sub-miniature hot wire probes could be operated successfully on this CTA for the first time.

These theoretical attempts to predict the frequency response of a CTA circuit are accompanied by experimental approaches. Bonnet and de Roquefort [4] heated the wire periodically by a perturbation voltage as well as laser heating to determine the frequency response. Weiss et al. [49] used the aforementioned square wave test and interpreted its power spectrum as a measure for the frequency response curve. Hutchins et al. [20] exploited the well-defined frequency content of pipe flow at different operating pressures to obtain frequency response curves without artificial heating. They were able to create flows of almost identical Reynolds number, but different frequency content and could deduce the frequency-response curves for different circuits and wires. They compared several anemometer circuits and wires and found that the frequency responses are non-constant at frequencies as low as 500 Hz. For the combination of CTA circuit and wire used in the present study, they report an attenuation between 400 Hz and 7 kHz followed by a strong amplification of the signal. We therefore cannot assume a flat frequency response for our measurements and address these effects below.

The energy spectrum measured by a hot wire is influenced by the effects of finite wire length. Length scales smaller than the sensor’s sensing lengths l will be attenuated, but also larger wavenumbers are influenced. Wynaard [51] used a Pao model spectrum [29] to investigate this attenuation of small scales. These results were reviewed in Ref. [28] indicating that for $l/\eta = 2$, the atten-

uation of the one-dimensional spectrum is still minimal at $k\eta \sim 0.3$, which was supported Ashok et al. [1]. Sadeghi et al. [34] used sub-miniature hot wires (NSTAPs) as a benchmark and found that spatial filtering of the energy spectrum is minimal for $l/\eta < 3.7$ at $k\eta < 0.1$.

In this study we used conventional hot wires of sensing length 450 μm for pressures below 2 bar, as well as Nanoscale Thermal Anemometry Probes (NSTAP) of sensing length 30 μm provided by Princeton University with a Dantec Dynamics StreamWare CTA circuit. The NSTAP is a 100 nm thick, 2.5 μm wide, and 30 or 60 μm long free-standing platinum film supported by a silicon structure and soldered to the prongs of a Dantec hot wire. The production process and characteristics are detailed in Refs. [2, 13, 25, 45]. For the conventional hot wire $l/\eta < 5$ in all cases and for the NSTAP $l/\eta < 3$. Therefore, η cannot be fully resolved in all cases. However, the bottleneck effect is typically found around 100η . The aforementioned references show that we can regard the distortions due to finite wire length as minor in this part of the energy spectrum.

To summarize, the spatial resolution of our measurement instruments is sufficient to study the R_λ -dependence of the bottleneck effect. Nevertheless the nonlinear frequency response of the circuitry remains. Here we describe a procedure that takes the response into account and thus removes this systematic measurement error.

III. RELATIVE SPECTRA

A. The concept

As outlined above, systematic errors influence the energy spectra recorded with a hot-wire anemometer as outlined above. Formally, this means that the one-dimensional energy spectrum $E_{11}(f)$ is distorted by a frequency-dependent transfer function $T(f)$:

$$E_M(f) = E_{11}(f)T(f)$$

$T(f)$ describes the effects of the thermal wire response, which depends on pressure and speed, and the response of the constant temperature anemometry circuit. Ideally, $T(f)$ is a constant over the whole range of relevant frequencies, but the evidence detailed above indicates a complex shape of amplification and attenuation of the signal. In this study we do not make any attempt to find $T(f)$. Instead, we control its effects by keeping $T(f)$ the same for several flows at different R_λ .

To ensure that the spectra only differ because of changes in the turbulent fluctuation and not because of the frequency response curve of the anemometer, we need to ensure that the response curve $T(f)$ is unaltered between spectra. We achieve this in two steps. The ambient pressure might influence the heat transfer of the wire and therefore $T(f)$. Furthermore, $T(f)$ is influenced by the

CTA tuning (in particular the overheat), and the sensor itself. Therefore, we fix the ambient pressure within a set of spectra (a 'Dataset') and measure using the same sensor and the same CTA settings.

The second step is to ensure that a given $k\eta$ is influenced by the same part of the frequency response curve $T(f)$. Thus, we need to fix the position of a spectral feature in frequency space. This means that the mean velocity U must be the same within one Dataset. $T(f)$ mainly distorts the small-scale end of the spectrum [15, 20, 28, 30, 37, 48–50], whose location in frequency space at a given U is determined by the kinematic viscosity ν . ν is fixed within a Dataset because the pressure remains constant.

We can, however, change the energy injection scale and thus the R_λ with the autonomous active grid. This way we can conduct measurements at different R_λ . Ultimately, we can eliminate $T(f)$ by relating each spectrum to a reference spectrum:

$$\begin{aligned} \frac{E_M^i(f)}{E_M^{\text{Ref}}(f)} &= \frac{E_{11}^i(f)T^i(f)}{E_{11}^{\text{Ref}}(f)T^{\text{Ref}}(f)} \\ &= \frac{E_{11}^i(f)T(f)}{E_{11}^{\text{Ref}}(f)T(f)} = \frac{E_{11}(kU/2\pi)}{E_{11}^{\text{Ref}}(kU/2\pi)}. \end{aligned} \quad (2)$$

In the following we call the ratio of a spectra divided by a reference spectrum in the frequency domain, relative spectrum.

B. Results

We created three sets of spectra that have identical $T(f)$ each. We call these sets 'Datasets'. Tab. I shows important parameters for each spectrum. Note that L changes significantly within a given dataset leading to changes in R_λ , while $f_\eta = U/\eta$ remains almost constant within the dataset. This indicates that we changed R_λ only by increasing the large scales, while keeping all small-scale features of the spectrum at the same frequency f_F . For example, in Dataset 2, the peak of the spectral bump always lies at a frequency of ~ 700 Hz, whereas the beginning of the inertial range spans a factor of 4 in frequency (2 to 8 Hz). This exemplifies the excellent control over R_λ permitted by the autonomous active grid as indicated in Fig. 2.

The lower graphs of Figs. 3 - 5 show the spectra from each of the respective datasets divided by the reference spectrum E_{11}^{Ref} . E_M^{Ref} is plotted pre-compensated in the upper graphs of the respective figure. Note that the absolute spectra in the upper graphs are multiplied by an unknown transfer function $T(f)$ accounting for probe effects and therefore can not be used to reliably measure the features of the bottleneck. However, the relative curves are corrected and allow a measurement. The graphs are the result of a smoothing procedure and error estimate detailed in the appendix. In brief, the spectra were smoothed using a $1/f$ octave filtering and the error

Dataset	R_λ	$p(\text{bar})$	$U(\text{m/s})$	$u(\text{m/s})$	Sensor	$L = \int C(r)dr$ (m)	η (μm)	f_η (kHz)
1	193	1.5	2.75	0.04	Regular HW	0.12	277	9.9
1	500	1.5	2.41	0.14	Regular HW	0.19	139	17.3
1	690	1.5	2.41	0.18	Regular HW	0.23	127	19.0
1	735	1.5	2.65	0.19	Regular HW	0.27	127	20.9
1	757	1.5	2.43	0.20	Regular HW	0.24	116	20.9
1	989	1.5	2.72	0.22	Regular HW	0.32	120	22.7
1	1305	1.5	2.28	0.34	Regular HW	0.70	91	25.1
2	1308	5.95	3.64	0.20	NSTAP 1	0.19	37	98.4
2	1539	5.95	3.68	0.22	NSTAP 1	0.24	36	102.2
2	2385	5.97	3.64	0.35	NSTAP 1	0.33	28	130.0
2	2704	5.97	3.61	0.40	NSTAP 1	0.43	26	138.9
3	3641	14.62	3.75	0.44	NSTAP 2	0.38	10	375.0
3	3821	14.71	3.83	0.41	NSTAP 2	0.27	12	319.2
3	4247	14.65	3.97	0.53	NSTAP 2	0.54	9.2	431.5
3	5130	14.66	4.01	0.58	NSTAP 2	0.86	9.1	440.7

Table I. Properties of all spectra. All spectra of a Dataset are distorted by the same function $T(f)$ describing the sensor- and instrument-induced bias. This is ensured by changing R_λ only through large scales L and fixing the position of the small scales in frequency space indicated by f_η . A reference spectrum has been chosen from each dataset, which is emboldened in this table.

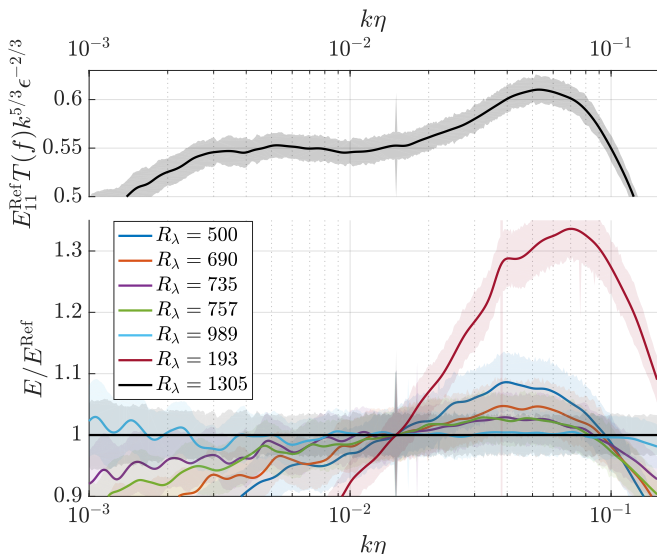


Figure 3. Reference spectrum at $R_\lambda = 989$ (upper plot) and relative spectra from Dataset 1. The data have been collapsed at $k\eta = 0.015$, which we defined as the beginning of the bottleneck region. We identified the peaks in the relative spectra with the bottleneck peak of the absolute spectra. The peak height decreased with increasing R_λ and different spectra of similar R_λ result in very similar relative spectra as expected. Furthermore, the slope of the spectrum at $k\eta < 0.015$ seems to decrease with R_λ . The shaded areas are a measure of the noise level.

is related to the noise level removed by the smoothing procedure. The spectra have been divided by the reference spectrum in the frequency domain and collapsed at $k\eta = 0.015$ afterwards to simplify interpretation.

While in Dataset 3 the beginning of the bottleneck region around $k\eta = 0.015$ is accompanied by a change

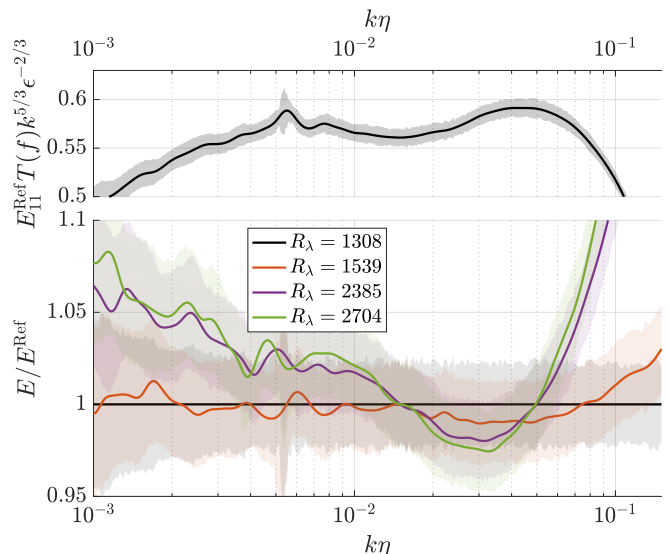


Figure 4. Reference spectrum at $R_\lambda = 1308$ (upper plot) and relative spectra from Dataset 2. The trends in peak height and slope from Fig. 3 continue.

in the shape of the relative spectra, this point cannot be identified in the relative spectra of Datasets 1 and 2. The relative spectra seem to follow approximately straight lines in our semilogarithmic plot, i.e. $E_{11}/E_{11}^{\text{Ref}} \sim \zeta(R_\lambda) \log(k\eta)$. The slope of these lines appears to become less steep with R_λ , leading to the prefactor $\zeta(R_\lambda)$. In the following we concentrate on the bottleneck effect found at $k\eta > 0.015$ for the remainder of this section.

The location of the spectral bump forming the bottleneck effect in relative spectra is not obvious. However, when considering the background noise, the peak location

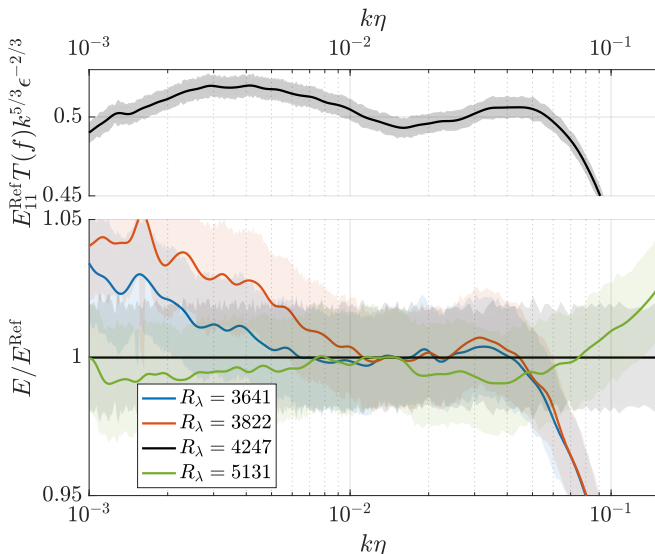


Figure 5. Reference spectrum at $R_\lambda = 4247$ (upper plot) and relative spectra from Dataset 3. Unlike in Datasets 1 and 2, the beginning of the bottleneck region around $k\eta = 0.015$ is identifiable in the relative spectra as a local extremum.

is not the major source of error. E.g. for $R_\lambda = 1539$, all points between $0.015 < k\eta < 0.07$ are within the error-band at $k\eta = 0.05$. We therefore define the extremum in the relative spectrum between $0.015 < k\eta < 0.08$ as the relative height h of the bottleneck effect. This has the additional advantage to be independent of the errors in the estimate of η . To preclude biases from this definition, we repeat our analysis with different definitions of the relative bottleneck height in Fig. (11) in the appendix.

Finally, the measured bottleneck height cannot depend on which spectrum is chosen as reference. We have calculated the bottleneck height with all possible choices of E_{11}^{Ref} and found our results to be largely independent of that choice (see Appendix for details).

Fig. 6 shows the bottleneck height - defined as above - as a function of $R_\lambda/R_\lambda^{Ref}$ within each dataset. The data shows a trend towards smaller peak heights in the relative spectrum with increasing R_λ . The data follows the numerical data we have compiled from various sources [6, 7, 22, 54]. We have analyzed the data from Buaria et al. [6] at R_λ up to 650 ($R_\lambda/R_\lambda^{Ref} < 1$). The increased small-scale resolution in comparison to [10] seems to have no noticeable impact on the bottleneck. Therefore, this data at is practically the same as the one used by Donzis & Sreenivasan [10] for our purposes. The data from $R_\lambda = 1300$ ($R_\lambda/R_\lambda^{Ref} = 1$) was reported in Ref. [7]. The numerical data at $R_\lambda/R_\lambda^{Ref} \approx 1.9$, which corresponds to $R_\lambda = 2340$, is the highest R_λ reported by Ishihara et al. [22]. The relative spectra of the numerical data were analyzed equivalently to the experimental data and the spectrum at $R_\lambda = 1300$ was chosen as a reference spectrum.

When excluding the lowest R_λ , the experimental data

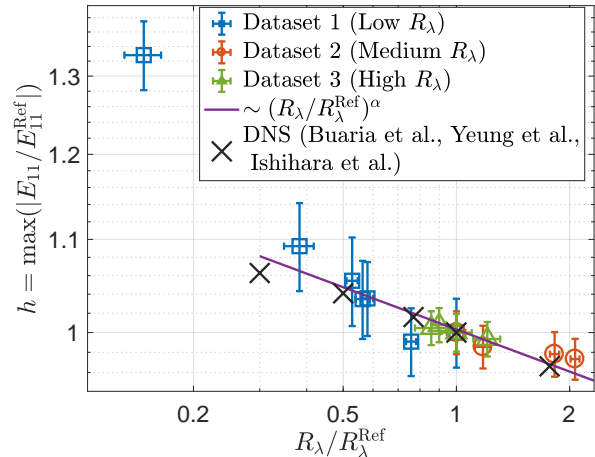


Figure 6. Bottleneck height relative to the reference spectrum for all datasets as a function of $R_\lambda/R_\lambda^{Ref}$. The reference spectra have bottleneck height 1. Numerical simulations from Buaria et al. [6] at R_λ up to 650 ($R_\lambda/R_\lambda^{Ref} < 1$), Buaria et al. [7] ($R_\lambda = 1$) and Ishihara [22] ($R_\lambda > 1$) are added for reference. A power law is fitted to the experimental data with the lowest $R_\lambda/R_\lambda^{Ref}$ excluded. $(R_\lambda/R_\lambda^{Ref})^{-0.061 \pm 0.007}$ is a good description of the experimental data over one decade of R_λ (from 500 to 5000) and agrees with the numerical simulations as well. This power law is used in Fig. 7 to combine Datasets 2 and 3.

is in agreement with the power law of

$$h \sim (R_\lambda/R_\lambda^{Ref})^{-0.061 \pm 0.007}.$$

The fit was obtained by a bootstrap procedure based on the error bars.

The spectrum at $R_\lambda = 193$ follows the general trend of decreasing peak height with R_λ , but its peak differs substantially from the predictions. The absolute spectrum (not shown) exhibits no signs of a $5/3$ -scaling, and consequently the bottleneck region cannot be clearly separated from the rest of the spectrum. This is substantially different from the other spectra, where the end of the integral range could always be observed in the absolute spectra and we therefore are not surprised that the relative spectrum at $R_\lambda = 193$ deviates from the remainder of the data. This spectrum has consequently been ignored in our interpretation.

Further, we can change R_λ only by a factor of 5 through the autonomous active grid. While Dataset 1 and 2 each feature a spectrum at the same R_λ , there is a gap between the highest R_λ of Dataset 2 (2704) and the lowest of Dataset 3 (3641). To plot h as a function of R_λ alone, we use the aforementioned power law fit from Fig. 6, i.e. we assume $h(R_\lambda = 3641) = h(R_\lambda = 3641)(3641/2704)^{-0.061}$ to arrive at Fig. 7.

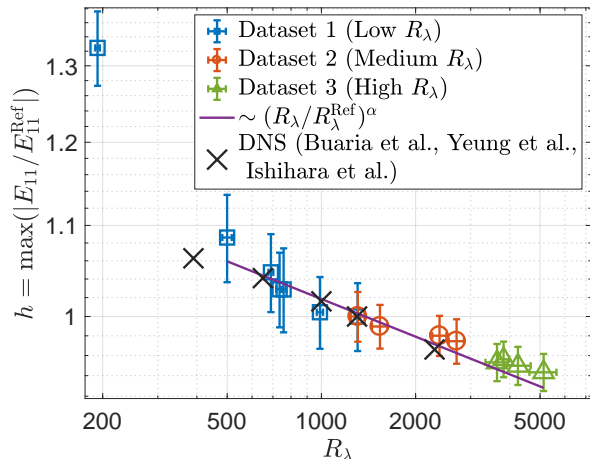


Figure 7. We have shifted Dataset 3 from Fig. 6 under the assumption of a power law $\sim (R_\lambda/R_\lambda^{\text{Ref}})^\alpha$ with $\alpha = -0.061 \pm 0.007$, i.e. the position of Dataset 3 with respect to the other Datasets is constructed artificially from the power law in Fig. 6. We have no physical justification for this power law and stress that the position of Dataset 3 in this figure is speculative.

IV. DISCUSSION

In this paper we studied the spectra of a turbulent wind tunnel flow of R_λ between 193 and 5131. We have used regular hot-wires as well as NSTAPs with a state-of-the-art constant temperature anemometer to record single-point two-time statistics of the turbulent fluctuations, in particular energy spectra. However, such spectra can be heavily influenced by non-ideal frequency responses of the circuit. The frequency response is particularly complicated when operating sub-miniature wires like the NSTAP with a CTA [20, 37]. A constant current anemometer (CCA) might perform better in this respect, because the frequency response is limited only by the thermal lag of the wire and no feedback loop is involved. Still, this comes at the expense of a variable wire temperature and -resistance.

In an attempt to interpret CTA data suffering from a non-flat frequency response, we consider energy spectra relative to a reference spectrum. Such an analysis significantly restricts the phenomena that can be observed. The bump in the energy spectrum at the transition from the inertial to the dissipation range can still be identified in the relative spectra as a local extremum beyond $k\eta = 0.015$.

To the best of our knowledge, no other wind tunnel achieves $R_\lambda > 5000$ in a gas. Moreover, we do not know of any other quantitative study of the scaling of the bottleneck effect with R_λ in a laboratory experiment. We attribute this to the difficulties one faces when interpreting energy spectra from CTA measurements at relatively high frequencies: The spectrum is strongly influenced by

the CTA circuitry and these influences are hard to quantify or eliminate.

With the aforementioned procedures we are able to extract information about the bottleneck effect from instrument-distorted hot wire spectra. We find indications that the bottleneck effect decreases up to $R_\lambda \sim 5000$. We fit a power law of $(R_\lambda/R_\lambda^{\text{Ref}})^{-\alpha}$ with $\alpha = 0.061 \pm 0.007$, which is close to the value of $(R_\lambda)^{-0.04}$ found by Donzis & Sreenivasan [10]. Their numerical results are in general in good agreement with our experimental data, lending support to the experiment and data analysis procedure. Our data equally supports Verma & Donzis [47], who predict that the bottleneck scales as $h \sim 1 - \gamma(1.5 \log_2(R_\lambda))^{2/3}$.

We attempt to plot the relative bottleneck height as a function of R_λ alone. This requires the assumption that the aforementioned power law holds and can be extrapolated. Such an assumption is highly speculative and the results should be considered as such.

We can not quantify the absolute height of the bottleneck bump. Yet, we can argue that if the relative spectra are still changing with R_λ in the relevant region, the effect has not completely vanished. We can find a systematic decrease of the peak in the relative spectra for $R_\lambda < 3000$. The data for $R_\lambda > 3000$ in Dataset 3 is inconclusive. A small, decreasing trend can be found, consistent with the power law fit. However, the differences in height are so small compared to the error bars that the claim of a constant bottleneck height at $R_\lambda > 3000$ would also be supported by the data, especially when considering alternative definitions of the bottleneck height in relative spectra as in Fig. 11 found in the appendix. This is not in contradiction to the atmospheric spectra mentioned above, as they have an even higher R_λ . Further, we note that a bottleneck effect might not show up as a peak in a $5/3$ -compensated spectrum, yet might be present when compensating by an intermittency-corrected slope $-(5/3 + \beta)$. In this case, the bottleneck effect would still be visible in the relative spectrum. However, the claim that the bottleneck height does not change with R_λ for $R_\lambda > 3000$ is not ruled out by the data.

As far as this study is concerned, the data matches the predictions of Verma & Donzis [47]: The bottleneck height decreases with increasing R_λ , but relatively high R_λ are necessary to make the effect vanish completely. Based on nonlinear and nonlocal shell-to-shell energy transfer Verma & Donzis [47] estimate that the bottleneck is basically absent for $R_\lambda > 10^4$, but acknowledge that this might be an overestimate. While lending support to existing studies of the bottleneck effect, especially [10] and theories that incorporate a R_λ -dependence of the peak height, an investigation of the effect in terms of absolute measurements of spectra seems necessary to confirm these claims experimentally. With subminiature probes of low thermal lag, such a study might be possible with a constant current anemometer, whose frequency response is intrinsically more simple.

V. CONCLUSIONS

Hot-wire measurements of high-wavenumber parts of the energy spectrum in a turbulent flow such as the bottleneck effect are distorted by non-flat frequency responses typical for constant temperature anemometers. When the experiment allows for a change in R_λ through the forcing mechanism alone, the R_λ -dependence at such high wavenumbers can be investigated. We have used an active grid to fix the frequency at which the bottleneck effect occurs. Thereby the bottleneck effect was always subject to the same systematic errors. By considering spectra relative to a reference spectrum, we found a R_λ -scaling of the bottleneck effect.

We have found indications that the bottleneck effect

gets weaker with increasing R_λ . The data are very similar to the results of DNS [10] and a theory [47]. R_λ exceeds 5000 in the VDTT with an autonomous active grid, which is unprecedented in any wind tunnel. At $R_\lambda > 3000$ our data supports a further decrease of the bottleneck height with R_λ as well as a constant or absent bottleneck.

ACKNOWLEDGEMENTS

The operation of the experiment would be impossible without the help and expertise of A. Kubitzek, A. Kopp, A. Renner, U. Schminke and O. Kurre. The NSTAPs were generously provided by M. Hultmark and Y. Fan. We thank P. K. Yeung and T. Ishihara for providing the numerical data. We thank D. Lohse and P. Roche for useful comments.

-
- [1] Ashok, A., Bailey, S.C.C., Hultmark, M., Smits, A.J.: Hot-Wire Spatial Resolution Effects in Measurements of Grid-Generated Turbulence. *Experiments in Fluids* **53**(6), 1713–1722 (2012). doi:10.1007/s00348-012-1382-5
- [2] Bailey, S.C.C., Kunkel, G.J., Hultmark, M., Vallikivi, M., Hill, J.P., Meyer, K.A., Tsay, C., Arnold, C.B., Smits, A.J.: Turbulence Measurements using a Nanoscale Thermal Anemometry Probe. *Journal of Fluid Mechanics* **663**, 160–179 (2010). doi:10.1017/S0022112010003447
- [3] Bodenschatz, E., Bewley, G.P., Nobach, H., Sinhuber, M., Xu, H.: Variable Density Turbulence Tunnel Facility. *Review of Scientific Instruments* **85**(9), 093908 (2014). doi:10.1063/1.4896138
- [4] Bonnet, J.P., Alziary de Roquefort, T.: Determination and Optimization of Frequency Response of Constant Temperature Hot-Wire Anemometers in Supersonic Flows. *Review of Scientific Instruments* **51**(2), 234–239 (1980). doi:10.1063/1.1136180
- [5] Bourgoin, M., Baudet, C., Kharche, S., Mordant, N., Vandenberghe, T., Sumbekova, S., Stelzenmuller, N., Aliseda, A., Gibert, M., Roche, P.E., Volk, R., Barois, T., Caballero, M.L., Chevillard, L., Pinton, J.F., Fiabane, L., Delville, J., Fourment, C., Bouha, A., Danaila, L., Bodenschatz, E., Bewley, G., Sinhuber, M., Segalini, A., Örlü, R., Torrano, I., Mantik, J., Guariglia, D., Uruba, V., Skala, V., Puczyłowski, J., Peinke, J.: Investigation of the small-scale statistics of turbulence in the Modane S1MA wind tunnel **9**(2), 269–281. doi:10.1007/s13272-017-0254-3.
- [6] Buaria, D., Pumir, A., Bodenschatz, E., Yeung, P.K.: Extreme velocity gradients in turbulent flows. under Review
- [7] Buaria, D., Sawford, B.L., Yeung, P.K.: Characteristics of backward and forward two-particle relative dispersion in turbulence at different Reynolds numbers. *Physics of Fluids* **27**(10), 105101. doi:10.1063/1.4931602.
- [8] Comte-Bellot, G.: Hot-wire anemometry **8**(1), 209–231. doi:10.1146/annurev.fl.08.010176.001233.
- [9] Dobler, W., Haugen, N.E.L., Yousef, T.A., Brandenburg, A.: Bottleneck Effect in Three-Dimensional Turbulence Simulations. *Physical Review E* **68**(2) (2003). doi:10.1103/PhysRevE.68.026304
- [10] Donzis, D.A., Sreenivasan, K.R.: The best Bottleneck Effect and the Kolmogorov Constant in Isotropic Turbulence. *Journal of Fluid Mechanics* **657**, 171–188 (2010). doi:10.1017/S0022112010001400
- [11] Falkovich, G.: Bottleneck Phenomenon in Developed Turbulence. *Physics of Fluids* **6**(4), 1411–1414 (1994). doi:10.1063/1.868255
- [12] Fan, Y.: High Resolution Instrumentation for Flow Measurements. Thesis, Princeton University, Princeton, NJ, USA (2017)
- [13] Fan, Y., Arwatz, G., Van Buren, T.W., Hoffman, D.E., Hultmark, M.: Nanoscale Sensing Devices for Turbulence Measurements. *Experiments in Fluids* **56**(138) (2015). doi:10.1007/s00348-015-2000-0
- [14] Fefferman, C.L.: Existence and smoothness of the navier-stokes equation **57**, 67. Citation Key: fefferman2006existence
- [15] Freymuth, P.: Frequency Response and Electronic Testing for Constant-Temperature Hot-Wire Anemometers. *J. Phys. E: Sci. Instrum.* **10**(7), 705 (1977). doi:10.1088/0022-3735/10/7/012
- [16] Frisch, U., Kurien, S., Pandit, R., Pauls, W., Ray, S.S., Wirth, A., Zhu, J.Z.: Hyperviscosity, Galerkin Truncation, and Bottlenecks in Turbulence. *Phys. Rev. Lett.* **101**(14), 144501 (2008). doi:10.1103/PhysRevLett.101.144501
- [17] Griffin, K.P., Wei, N.J., Bodenschatz, E., Bewley, G.P.: Control of Long-Range Correlations in Turbulence. *Experiments in Fluids* **under review** (2018)
- [18] Gulitski, G., Kholmyansky, M., Kinzelbach, W., Lüthi, B., Tsinober, A., Yorish, S.: Velocity and Temperature Derivatives in high-Reynolds-number Turbulent Flows in the Atmospheric Surface Layer. Part 1. Facilities, methods and some general results. *Journal of Fluid Mechanics* **589** (2007). doi:10.1017/S0022112007007495
- [19] Hideharu, M.: Realization of a Large-Scale Turbulence Field in a Small Wind Tunnel. *Fluid Dynamics Research* **8**(1), 53–64 (1991). doi:10.1016/0169-5983(91)90030-M
- [20] Hutchins, N., Monty, J.P., Hultmark, M., Smits, A.J.: A Direct Measure of the Frequency Response of Hot-

- Wire Anemometers: Temporal Resolution Issues in Wall-Bounded Turbulence. *Experiments in Fluids* **56**(18) (2015). doi:10.1007/s00348-014-1856-8
- [21] Ishihara, T., Kaneda, Y., Yokokawa, M., Itakura, K., Uno, A.: Energy Spectrum in the Near Dissipation Range of High Resolution Direct Numerical Simulation of Turbulence. *Journal of the Physical Society of Japan* **74**(5), 1464–1471 (2005). doi:10.1143/JPSJ.74.1464
- [22] Ishihara, T., Morishita, K., Yokokawa, M., Uno, A., Kaneda, Y.: Energy Spectrum in High-Resolution Direct Numerical Simulations of Turbulence. *Physical Review Fluids* **1**(8) (2016). doi:10.1103/PhysRevFluids.1.082403
- [23] Khurshid, S., Donzis, D.A., Sreenivasan, K.R.: Energy Spectrum in the Dissipation Range. *Physical Review Fluids* **3**(8) (2018). doi:10.1103/PhysRevFluids.3.082601
- [24] Kolmogorov, A.: The Local Structure of Turbulence in Incompressible Viscous Fluid for Very Large Reynolds Numbers. *Akademiia Nauk SSSR Doklady* **30**, 301–305
- [25] Kunkel, G., Arnold, C., Smits, A.: Development of NSTAP: Nanoscale Thermal Anemometry Probe. *American Institute of Aeronautics and Astronautics* (2006). doi:10.2514/6.2006-3718
- [26] Kurien, S., Taylor, M.A., Matsumoto, T.: Cascade Time Scales for Energy and Helicity in Homogeneous Isotropic Turbulence. *Phys. Rev. E* **69**(6), 066313 (2004). doi:10.1103/PhysRevE.69.066313
- [27] Lohse, D., Mueller-Groeling, A.: Bottleneck effects in turbulence: Scaling phenomena in r - versus p -space. *Physical Review Letters* **74**(10), 1747–1750. doi:10.1103/PhysRevLett.74.1747.
- [28] McKeon, B., Comte-Bellot, G., Foss, J., Westerweel, J., Scarano, F., Tropea, C., Meyers, J., Lee, J., Cavone, A., Schodl, R., Koochesfahani, M., Andreopoulos, Y., Dahm, W., Mullin, J., Wallace, J., Vukoslavčević, P., Morris, S., Pardyjak, E., Cuerva, A.: Velocity, Vorticity, and Mach Number. In: C. Tropea, A.L. Yarin, J.F. Foss (eds.) *Springer Handbook of Experimental Fluid Mechanics*, pp. 215–471. Springer Berlin Heidelberg, Berlin, Heidelberg (2007). doi:10.1007/978-3-540-30299-5_5
- [29] Pao, Y.: Structure of Turbulent Velocity and Scalar Fields at Large Wavenumbers. *The Physics of Fluids* **8**(6), 1063–1075. doi:10.1063/1.1761356.
- [30] Perry, A.E., Morrison, G.L.: A Study of the Constant-Temperature Hot-Wire Anemometer. *Journal of Fluid Mechanics* **47**(3), 577 (1971). doi:10.1017/S0022112071001241
- [31] Pietropinto, S., Poulain, C., Baudet, C., Castaing, B., Chabaud, B., Gagne, Y., Hebral, B., Ladam, Y., Lebrun, P., Pirotte, O., Roche, P.: Superconducting Instrumentation for high Reynolds Turbulence Experiments with low Temperature gaseous Helium. *Physica C: Superconductivity* **386**, 512–516. doi:10.1016/S0921-4534(02)02115-9.
- [32] Rousset, B., Bonnay, P., Diribarne, P., Girard, A., Poncet, J.M., Herbert, E., Salort, J., Baudet, C., Castaing, B., Chevillard, L., Daviaud, F., Dubrulle, B., Gagne, Y., Gibert, M., Hebral, B., Lehner, T., Roche, P.E., Saint-Michel, B., Bon Mardion, M.: Superfluid high REynolds von Kármán experiment. *Review of Scientific Instruments* **85**(10), 103908 (2014). doi:10.1063/1.4897542
- [33] Saddoughi, S.G., Veeravalli, S.V.: Local Isotropy in Turbulent Boundary Layers at high Reynolds number. *Journal of Fluid Mechanics* **268**, 333 (1994). doi:10.1017/S0022112094001370
- [34] Sadeghi, H., Lavoie, P., Pollard, A.: Effects of Finite Hot-Wire Spatial Resolution on Turbulence Statistics and Velocity Spectra in a Round Turbulent Free Jet. *Experiments in Fluids* **59**(40) (2018). doi:10.1007/s00348-017-2486-8
- [35] Saint-Michel, B., Herbert, E., Salort, J., Baudet, C., Bon Mardion, M., Bonnay, P., Bourgoïn, M., Castaing, B., Chevillard, L., Daviaud, F., Diribarne, P., Dubrulle, B., Gagne, Y., Gibert, M., Girard, A., Hébral, B., Lehner, T., Rousset, B., SHREK Collaboration: Probing Quantum and Classical Turbulence Analogy in von Kármán liquid Helium, Nitrogen, and Water Experiments. *Physics of Fluids* **26**(12), 125109 (2014). doi:10.1063/1.4904378
- [36] Salort, J., Chabaud, B., Leveque, E., Roche, P.E.: Energy cascade and the four-fifths law in superfluid turbulence. *Europhysics Letters* **97**(3), 34006. doi:10.1209/0295-5075/97/34006.
- [37] Samie, M., Watmuff, J.H., Van Buren, T., Hutchins, N., Marusic, I., Hultmark, M., Smits, A.J.: Modelling and Operation of Sub-Miniature Constant Temperature Hot-Wire Anemometry. *Measurement Science and Technology* **27**, 125301 (2016). doi:10.1088/0957-0233/27/12/125301
- [38] She, Z.S., Jackson, E.: On the Universal Form of Energy Spectra in Fully Developed Turbulence. *Physics of Fluids A: Fluid Dynamics* **5**(7), 1526–1528 (1993). doi:10.1063/1.858591
- [39] Sinhuber, M., Bewley, G.P., Bodenschatz, E.: Dissipative Effects on Inertial-Range Statistics at High Reynolds Numbers. *Phys. Rev. Lett.* **119**(13), 134502. doi:10.1103/PhysRevLett.119.134502. Citation Key: PhysRevLett.119.134502 bibtex[publisher=American Physical Society;numpages=5]
- [40] Sinhuber, M., Bodenschatz, E., Bewley, G.P.: Decay of Turbulence at High Reynolds Numbers. *Physical Review Letters* **114**(3) (2015). doi:10.1103/PhysRevLett.114.034501
- [41] Sreenivasan, K.R., Dhruva, B.: Is There Scaling in High-Reynolds-Number Turbulence? *Progress of Theoretical Physics Supplement* **130**, 103–120 (1998). doi:10.1143/PTPS.130.103
- [42] Taylor, G.I.: The Spectrum of Turbulence. *Proc R Soc Lond A Math Phys Sci* **164**(919), 476. doi:10.1098/rspa.1938.0032.
- [43] Taylor, G.I.: Statistical Theory of Turbulence. *Proc R Soc Lond A Math Phys Sci* **151**(873), 421. doi:10.1098/rspa.1935.0158.
- [44] Tsuji, Y.: Intermittency Effect on Energy Spectrum in High-Reynolds Number Turbulence. *Physics of Fluids* **16**, L43–L46 (2004). doi:10.1063/1.1689931
- [45] Vallikivi, M., Smits, A.J.: Fabrication and Characterization of a Novel Nanoscale Thermal Anemometry Probe. *Journal of Microelectromechanical Systems* **23**(4), 899–907 (2014). doi:10.1109/JMEMS.2014.2299276
- [46] Verma, M.K., Ayer, A., Debliquy, O., Kumar, S., Chandra, A.V.: Local shell-to-shell energy transfer via nonlocal interactions in fluid turbulence. *Pramana - J Phys* **65**(2), 297. doi:10.1007/BF02898618.
- [47] Verma, M.K., Donzis, D.: Energy Transfer and Bottleneck Effect in Turbulence. *Journal of Physics A: Mathematical and Theoretical* **40**(16), 4401–4412 (2007). doi:10.1088/1751-8113/40/16/010

- [48] Watmuff, J.H.: An Investigation of the Constant-Temperature Hot-Wire Anemometer. *Experimental Thermal and Fluid Science* **11**, 117–134 (1995). doi: 10.1016/0894-1777(94)00137-W
- [49] Weiss, J., Knauss, H., Wagner, S.: Method for the Determination of Frequency Response and Signal to Noise Ratio for Constant-Temperature Hot-Wire Anemometers. *Review of Scientific Instruments* **72**, 1904 (2001). doi: 10.1063/1.1347970
- [50] Wood, N.B.: A Method for Determination and Control of the Frequency Response of the Constant-Temperature Hot-Wire Anemometer. *Journal of Fluid Mechanics* **67**(4), 769 (1975). doi:10.1017/S0022112075000602
- [51] Wyngaard, J.C.: Measurement of Small-Scale Turbulence Structure with Hot Wires. *Journal of Physics E: Scientific Instruments* **1**, 1105–1108 (1968). doi: 10.1088/0022-3735/1/11/310
- [52] Yakhot, V., Zakharov, V.: Hidden conservation laws in hydrodynamics; energy and dissipation rate fluctuation spectra in strong turbulence. *Physica D: Non-linear Phenomena* **64**(4), 379–394. doi:10.1016/0167-2789(93)90050-B.
- [53] Yeung, P.K., Sreenivasan, K.R., Pope, S.B.: Effects of Finite Spatial and Temporal Resolution in Direct Numerical Simulations of Incompressible Isotropic Turbulence. *Physical Review Fluids* **3**(6) (2018). doi: 10.1103/PhysRevFluids.3.064603
- [54] Yeung, P.K., Zhai, X.M., Sreenivasan, K.R.: Extreme events in computational turbulence. *Proc Natl Acad Sci USA* **112**(41), 12633. doi:10.1073/pnas.1517368112.

Appendix A: A brief description of the wind tunnel

The VDTT consists of two 11.7 m long straight cylindrical tubes connected by two elbows of center-line radius of 1.75 m. The tunnel was filled with sulfur-hexafluoride (SF6) at pressures between 1.5 and 15 bar for the measurements presented here.

The flow is propelled by a fan rotating at up to 24 Hz creating mean flow speeds of up to 5.5 m/s. It passes the first elbow and enters a heat exchanger, which removes any turbulent energy dissipated into heat and thus keeps the temperature in the tunnel constant. The rectangular cross-section of the heat exchanger is smoothly adapted to the tunnels circular geometry by contractions. The vertical slots of the heat exchanger are expected to destroy large-scales structure present in the flow. After the heat exchanger, the flow passes an 80 cm long expansion, which adapts it to the measurement section. While passing this expansion the flow is stabilized and homogenized by three consecutive meshes of ascending spacing. The flow enters a 9 m long measurement section through an 104 cm high active grid, which is directly followed by a 70 cm long expansion to the measurement section’s height of 117 cm. The measurement section is followed by another elbow and enters a second measurement section through another sequence of three meshes before being accelerated again by the fan.

Appendix B: Data Acquisition and Analysis Procedure

The NSTAPs were operated following largely [12] using a Dantec StreamLine 90C10 module within a 90N10 frame. The CTA bridge was set to a 1:1 ratio and the overheat is determined by an external resistor R_{ext} connected to the system. Typical overheat ratios $R_{\text{ext}}/R_{\text{Probe}}$ were 1.2-1.3, where $R_{\text{Probe}} \sim 100 \Omega$ denotes the probe cold resistance. The Dantec wires were used in a 1:20 bridge utilizing the internal automatics to set the overheat. The data was acquired in the following procedure: The hot wire frequency response and proper operation was tested on a very basic level using the square wave test built into the Dantec CTA-system. The hot-wire system was calibrated by scanning a range of mean flow speeds set by the fan frequency in the tunnel. We determined the mean flow speed through the differential pressure between a pitot tube and a static pressure probe. The differential pressure was picked up by a Siemens SITRANS differential pressure transducer/ We chose ~ 20 calibration points spaced by ~ 0.1 m/s. The probe voltage was recorded for 60 seconds along with the mean pressure difference, a voltage-velocity curve was calculated, and King’s law was fitted to the data. In between calibration points we waited for 45 seconds for the mean flow to become stationary. The data was recorded with a National Instruments NI PCI-6123 16-bit DAQ-Card at sampling rates of 60 or 200 kHz. Higher sampling rates were used for NSTAP measurements, where the CTA analog low-pass filter was set to 100 kHz. When using standard hot wires, the filter frequency was set to 30 kHz and the data was sampled at 60 kHz. The data was recorded in segments of 6 million voltage samples, each saved to disk in a 16-bit binary format.

We shall briefly outline the initial data analysis procedure used to obtain essential turbulence statistics as well as the power spectrum. Each of the following steps was carried out on each segment and the results were averaged over all files in the end. We used King’s law with parameters obtained from the calibration data to convert the voltages to velocities. Note that the shape of the energy-frequency spectrum is independent of the calibration, which is only required to obtain its absolute value. Because the analog filtering was not sufficient to filter out all noise, we low-pass filtered the data digitally using a sinc-Filter in forward and reverse directions. This introduces edge effects, which we remove by cutting the first and last 60 points of the time series. We then subtract the mean U from the velocity time series to obtain a time series of u . The remaining analysis is performed on this filtered dataset. The power spectra were calculated using MATLAB’s `fft` function, which is based on the FFTW-package. We calculate the correlation function using MATLAB’s `xcorr` function, which itself relies on the aforementioned fourier transform procedure as well as structure functions of order 1 to 8. Finally, we obtain histograms of velocity and voltage. We use Taylor’s Hy-

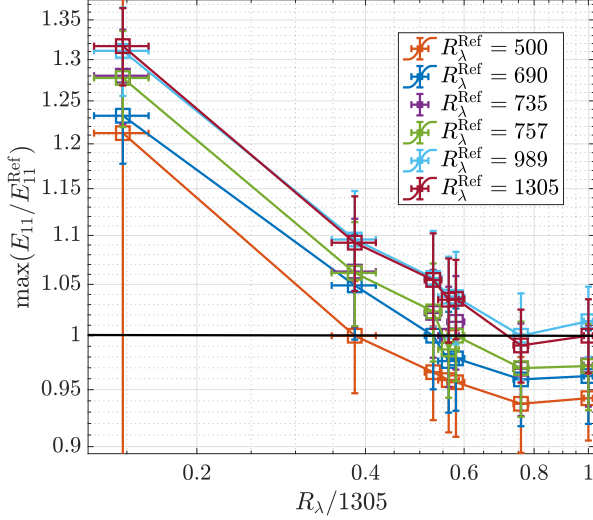


Figure 8. The bottleneck height in Dataset 1 with different choices of E_{11}^{Ref} . If the analysis is independent of the choice of reference spectrum, the graphs are parallel in this representation. Note that the reference spectrum always has bottleneck height 1.

pothesis, which assumes that a one-dimensional velocity field can be obtained from a time series by multiplying the time increments by the mean velocity: $\Delta x = \Delta t \cdot U$. The power spectra are normalized using the assumption that $\int E(k)dk = u^2$.

We routinely calculate basic turbulence quantities in different ways and check the results for consistency. The quantities R_λ , and η depend on the mean energy dissipation rate ε , which we measure using the third-order structure function $S_3(r) = \langle (u(x+r) - u(x))^3 \rangle = 4/5(\varepsilon r)$. The last step follows from the Navier-Stokes equations and is also predicted by Kolmogorov's 1941 theory. In practice we estimate $\varepsilon = \max(5/4 S_3/r)$ and check the result with $\varepsilon = 15\nu \int k^2 E(k)dk$, and $\varepsilon = \max(S_2^{3/2}/r)$. The integral length scale is calculated as $L = \int_0^\infty C(r)dr$, where $C(r) = \langle u(x+r)u(x) \rangle$ is the velocity auto-correlation function. Its error mainly stems from the ambiguous choice of the upper integration limit, which leads to a relative error about 10% in L .

Appendix C: Calculation and Cross-check of Relative Spectra

To obtain relative spectra, the initial spectrum consisting of 3 million points was downsampled to 50 000 logarithmically spaced datapoints. To remove the noise from these spectra, we have smoothed them using a fractional

octave smoothing algorithm. It multiplies the spectrum at each frequency with a Gaussian centered around the current frequency f_i with a width of $\sigma_i = (f_i/n)/\pi$, where n determines the smoothing level. Therefore, the

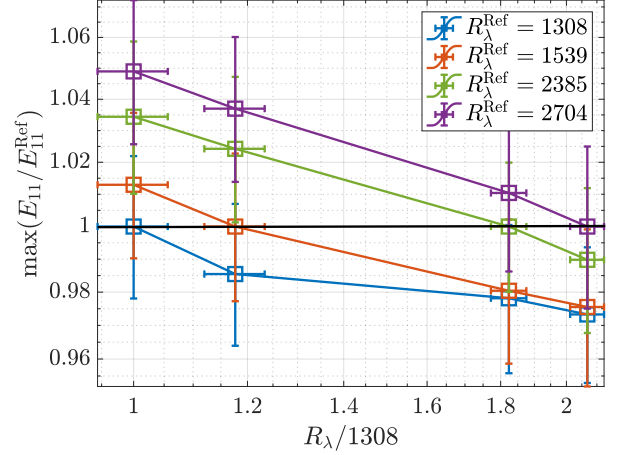


Figure 9. Same as Fig. 8 for Dataset 2

smoothing window is larger for higher frequencies. To estimate the noise level in the spectrum and the associated statistical error, we consider the data within $3\sigma_i$ of each frequency. We estimate the standard error as $\delta = 3\sqrt{\text{Var}/N}$, where N is the number of points considered and Var denotes their variance. Finally, the compensated spectra are calculated as $\psi(k) = E_{11}(k)k^{5/3}\varepsilon^{-2/3}$, which can be written as $\psi(f)$ by Taylor's Hypothesis. Finally, we divide the i -th spectrum in a dataset by the reference spectrum: $\psi_i(f)/\psi_{\text{Ref}}(f)$. The result is normalized at $k\eta = 0.015$ to remove offsets introduced by uncertainties in ε and to simplify comparisons.

An important cross-check of the technique is its independence from the choice of reference spectrum. To this end we have calculated the bottleneck effect according to the analysis outlined above for all possible choices of reference spectra. The results are shown in Figs. 8-10. They show the peak height in the relative spectra as a function of $R_\lambda/R_\lambda^{\text{Ref}}$. $R_\lambda/R_\lambda^{\text{Ref}}$ has been normalized to the value that was chosen in the main part of the paper to increase the clarity of the figures. If the analysis is independent of the choice of reference spectrum E_{11}^{Ref} , a different choice $E_{11}'^{\text{Ref}}$, should move the resulting curve by a factor of $E_{11}'^{\text{Ref}}/E_{11}^{\text{Ref}}$ upwards and $R_\lambda^{\text{Ref}}/R_\lambda'^{\text{Ref}}$ to the right. The latter is trivial and has been removed from Figs. 8-10 by the additional normalization. Thus, if the spectra are independent of the choice of reference spectrum, the bottleneck curves should be parallel. Figs. 8-10 show that this is valid in good approximation showing that the analysis is largely independent of the choice of reference spectrum within a dataset.

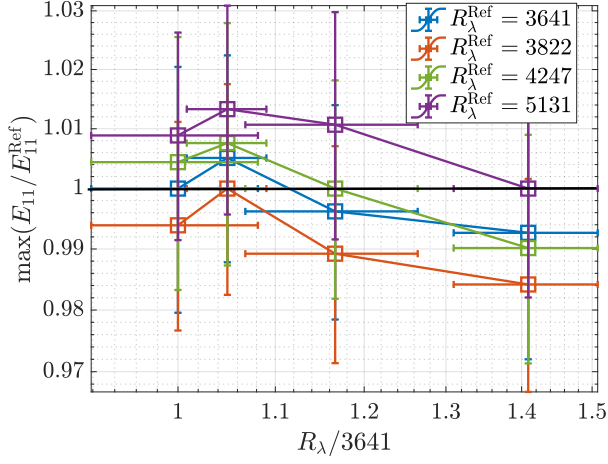


Figure 10. Same as Fig. 8 for Dataset 3

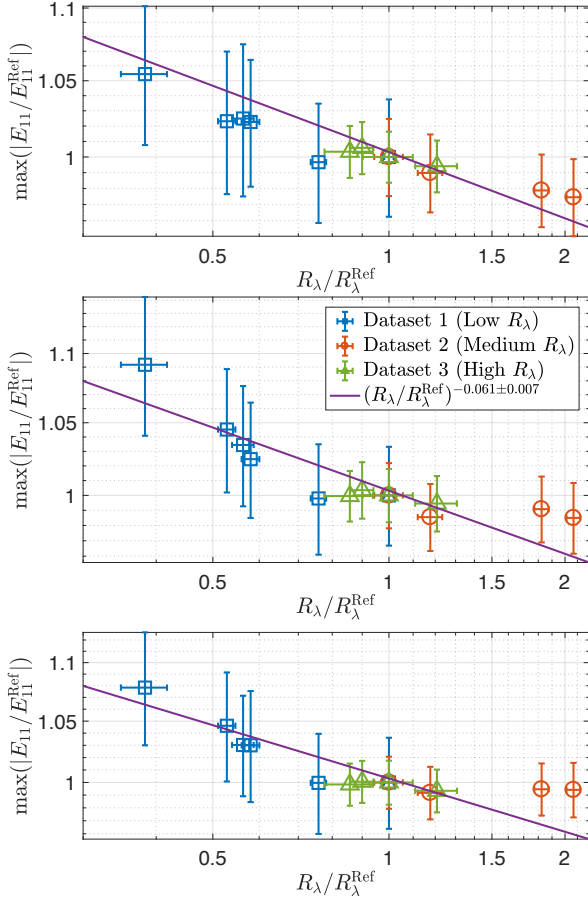


Figure 11. Bottleneck height as function of $R_{\lambda}/R_{\lambda}^{\text{Ref}}$ with different bottleneck definitions based on the height of the relative spectra at a fixed $k\eta$. The power law is the one found using the initial definition of the bottleneck height in Fig. 6. Upper graph: Bottleneck at $k\eta = 0.03$, middle graph at $k\eta = 0.04$, lower graph at $k\eta = 0.046$ (as predicted by DNS). Datasets 1 and 2 still follow the trend found in the main part. Dataset 3 is not inconsistent with the claim of a constant bottleneck height at $R_{\lambda} > 3000$.